Evanescent Light-Scattering Microscopy for Label-Free Interfacial Imaging: From Single Sub-100 nm Vesicles to Live Cells

Björn Agnarsson,*,† Anders Lundgren,† Anders Gunnarsson,†,# Michael Rabe,† Angelika Kunze,†,‡ Mokhtar Mapar,† Lisa Simonsson,† Marta Bally,† Vladimir P. Zhdanov,†,§ and Fredrik Höök*,†

†Division of Biological Physics, Department of Applied Physics, Chalmers University of Technology, SE-41296 Göteborg, Sweden, ‡Institute of Physical Chemistry, University of Göttingen, D-37077 Göttingen, Germany, and §Boreskov Institute of Catalysis, Russian Academy of Sciences, Novosibirsk 630090, Russia. #Present address: Discovery Sciences, AstraZeneca R&D, SE-43183 Mölndal, Sweden.

ABSTRACT Advancement in the understanding of biomolecular interactions has benefited greatly from the development of surface-sensitive bioanalytical sensors. To further increase their broad impact, significant efforts are presently being made to enable label-free and specific biomolecule detection with high sensitivity, allowing for quantitative interpretation and general applicability at low cost. In this work, we have addressed this challenge by developing a waveguide chip consisting of a flat silica core embedded in a symmetric organic cladding with a refractive index matching that of water. This is shown to reduce stray light (background) scattering and thereby allow for label-free detection of faint objects, such as individual sub-20 nm gold nanoparticles as well as sub-100 nm lipid vesicles. Measurements and theoretical analysis revealed that light-scattering signals originating from single surface-bound lipid vesicles enable characterization of their sizes without employing fluorescent lipids as labels. The concept is also demonstrated for label-free measurements of protein binding to and enzymatic (phospholipase A2) digestion of individual lipid vesicles, enabling an analysis of the influence on the measured kinetics of the dye-labeling of lipids required in previous assays. Further, diffraction-limited imaging of cells (platelets) binding to a silica surface showed that distinct subcellular features could be visualized and temporally resolved during attachment, activation, and spreading. Taken together, these results underscore the versatility and general applicability of the method, which due to its simplicity and compatibility with conventional microscopy setups may reach a widespread in life science and beyond.

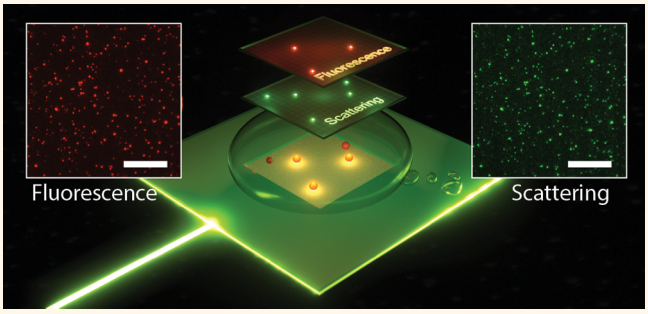

KEYWORDS: single molecule detection · label-free optical imaging · evanescent light · waveguide · biosensor · TIRF · TIR · scattering · fluorescence

Tracking biomolecular processes at or near a surface with sufficient sensitivity to reach the single-molecule level has emerged as a key component of basic science and is on the verge to be transferred to both medical diagnostics and drug discovery.[1−5] In this area, most work on time-resolved single-molecule imaging relies on labeling by fluorophores,[1−4,6] quantum dots,[7] or metallic nanoparticles.[8] Recently, label-free imaging of nanoscale dielectric supramolecular assemblies has also been accomplished using interferometric microscopy, a method which has been proven capable of detecting weakly scattering objects such as metallic nanoparticles down to 5 nm in diameter[9,10] as well as dielectric particles, such as viruses,[11−13] lipid vesicles[14] (∼50−100 nm in diameter), and most recently, even individual proteins.[15,16] Monitoring of surface binding of nanoparticles can also be efficiently carried out by more conventional microscopy techniques employing evanescent light to visualize objects in close proximity to a solid−liquid interface. Due to the high surface confinement of the illumination profile, significantly higher surface sensitivity can be achieved in this case compared to standard epi-illumination and confocal-based microscopy. This in turn

* Address correspondence to bjorn.agnarsson@chalmers.se, fredrik.hook@chalmers.se.

Received for review July 7, 2015 and accepted October 30, 2015.

Published online 10.1021/acsnano.5b04168

allows for interfacial binding to be probed, even in the presence of an appreciable amount of molecules in the bulk. Evanescent light illumination for applications in microscopy is most commonly generated using either prism- or objective-based total-internal reflection (TIR) illumination to excite fluorescently labeled entities close to the interface. TIR fluorescence (TIRF) microscopy can in this way be employed to observe binding of single fluorescent objects and even single chromophores.[17−20] In addition, TIR-based dark-field microscopy has recently been successfully used to detect scattered light originating from metallic and dielectric nanoparticles with reported sensitivities down ∼40 nm for metallic gold nanoparticles and ∼100 nm for dielectric virus particles.[21−23]

In addition to prism- and objective-based TIR illumination schemes, evanescent-light microscopy can be carried out using optical waveguides. By exposing a sample to the core layer of the waveguide, the evanescent part of the guided light will interact with the sample in a manner analogous to TIR illumination.[24−28] This mode of generating evanescent light has a number of advantages over conventional TIR illumination. In TIR microscopy, the penetration depth of the evanescent field is limited to around 100−200 nm from the surface, whereas for waveguides this depth can be tuned from below 100 nm to over a micron by varying the refractive indices and thicknesses of the core and/or cladding layers.[26] Planar waveguides also offer a more uniform illumination profile compared to TIR, and it can easily be extended over macroscopic areas limited only by the weak attenuation of the light in the waveguide. Importantly, in waveguide microscopy the paths of illumination and detection signals are perpendicular to each other. Consequently, no special requirements are placed on the objective used for signal collection, as is the case for in-lens TIR, where specially designed high magnification and high numerical aperture objectives with built-in optical path control must be employed. Most of the above-mentioned benefits of waveguide-based microscopy have already been demonstrated for fluorescently labeled probes,[26−30] while advantages offered by label-free detection through evanescent-light-induced scattering of nanoscopic particles has only been moderately explored, and so far with emphasis on synthetic grid film-like structures,[24] gold nanoparticles,[21,22] virions[23] and bacterial biofilms,[31] including attempts to study the forces acting on a particle through the evanescent field.[32] Herein, we introduce a simple waveguide-based technique for simultaneous fluorescent and high sensitivity scattering imaging of surface immobilized objects to investigate interfacial biological processes not studied in this label-free way before.

To improve the sensitivity upon evanescent-wave illumination and thereby enable label-free imaging of individual optically faint surface-bound biological entities, the stray light (background) scattering needs to be kept at minimum. For this purpose, we developed a sensing chip made from a planar symmetric three-layered (organic/inorganic/organic) waveguide structure consisting of a silica core layer embedded in a symmetric cladding made of an organic fluorinated polymer (CYTOP), with a refractive index (n = 1.34) closely matching that of water (n = 1.33). This refractive index matching together with the high smoothness of the core layer (root-mean-square surface roughness <1 nm) act to reduce stray light and enhance signal-to-background contrast, here utilized for detection of surface-bound nanoscopic biological particles in an aqueous environment *via* scattering of evanescent light.

To demonstrate the broad applicability and high sensitivity of the sensor system, we investigated the possibility of visualizing in parallel the scattered and fluorescent light from single lipid vesicles and studied certain aspects of biomolecular processes where label-free visualization of single lipid vesicles has remained challenging or where concerns have been raised regarding the influence on data interpretation of the fluorescence labels employed to reach the corresponding sensitivities. More specifically, the focus was placed on (i) determination of the size distribution of individual surface-bound lipid vesicles with nominal diameter around 150 nm, where a significant inhomogeneity in dye distribution among vesicles has been reported,[33] (ii) label-free detection of specific protein−receptor binding on single lipid vesicles, (iii) digestion of such vesicles using phospholipases, in which case previously employed dyes have dimensions similar to the size of the active sites,[34,35] and (iv) detection of single Au nanoparticle (∼18 nm in diameter) binding to functionalized surface-immobilized vesicles, demonstrating the applicability of the technique to use Au nanoparticles (NPs) instead of fluorophores for studying single molecular interactions. We also monitored the attachment and activation of unlabeled cells by tracking of attachment of platelets, derived from human blood, to a glass surface and their surface-induced activation and growth. In addition to the advances in the chip design, we extended the mathematical formalism for describing the evanescent-light scattering. The obtained results show that the waveguide setup, allowing combination of quantitative evanescent-based scattering and fluorescence imaging using ordinary microscopes, can serve as a powerful complement to fluorescence imaging and as an attractive complementary label-free imaging tool in cases when high sensitivity and surface confinement is advantageous.

RESULTS AND DISCUSSION

Symmetric propagation of the fundamental mode of a linearly polarized (TE, transverse electromagnetic) light (λ ∼ 532 nm) with an evanescent wave of

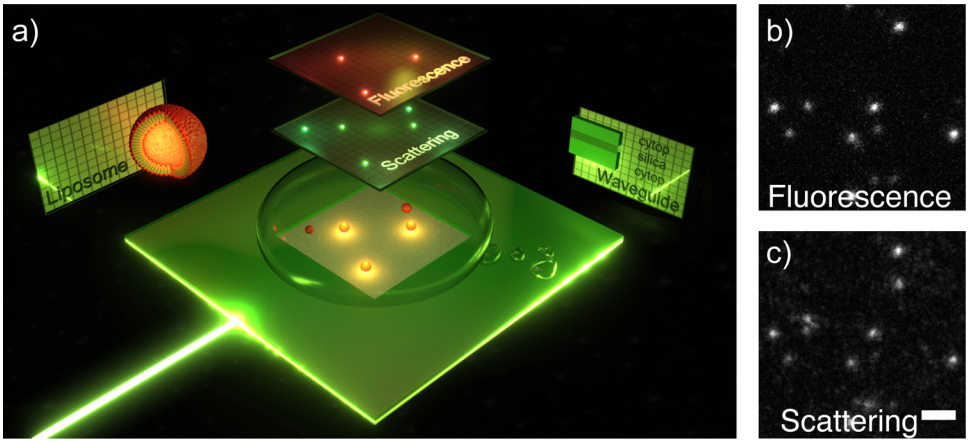

Figure 1. Schematic representation of the planar waveguide chip and detection of fluorescently labeled vesicles in fluorescence and scattering modes. (a) A single mode optical fiber was aligned to the facet of the planar waveguide and light (green) was coupled into the core layer of the chip. An opening (sample well) was formed in the upper cladding layer of the waveguide, into which a solution (drop) containing the specimen of interest was placed. The evanescent part of the in-coupled light interacts with objects present within the penetration depth of the evanescent light resulting in light scattering and, in the case of fluorescent objects, fluorescence generation. The emitted light was collected using a standard microscope objective in an upright or inverted configuration, or a combination of both, to reveal a scattered signal in the scattering image plane (green square) and/or a fluorescence signal in the fluorescence image plane (red/orange square). (b) Fluorescence and (c) scattering signals from the same 12 × 12 μm^2 area of the chip under identical illumination conditions, showing nominally 150 nm fluorescently labeled vesicles bound to the surface imaged with high- and low-pass filters, respectively, with cutoff wavelength of around 550 nm, *i.e.*, in between the excitation (532 nm) and emission (582 nm) wavelengths. The scale bar in (c) corresponds to 2 μm.

exponentially vanishing intensity with a decay length, δ, of ~130 nm confined to the core−liquid interface was generated using a waveguide chip consisting of a 400 nm thick silica core with a 4 μm thick CYTOP cladding layer on each side (see the Methods for details). This three-layered organic/inorganic/organic structure was fabricated on top of an optically flat supporting silicon substrate (Figure 1a), a configuration known to be compatible with a simple fiber-based end-fire coupling.[26] Exposure of the liquid sample under investigation to the evanescent illumination was accomplished by forming a quadratic opening in the upper cladding (sample well), enabling imaging of binding events at the interface of the silica core (Figure 1a).

Owing to the low stray-light scattering and since the optical paths of the excitation and emitted/scattered light are in this configuration decoupled, measurements could be performed by directly monitoring light scattering induced by the interaction between the evanescent light and surface-bound entities (scattering mode, indicated as green spots in the observation plane of Figure 1a). Using an appropriate filter, fluorescence signals (fluorescence mode, indicated as orange spots in the second observation plane of Figure 1a) could also be monitored either independently or in combination with the scattered signal. In this way, the binding of lipid vesicles (containing 1 wt % rhodamine-labeled lipids) with a nominal diameter of ~150 nm (see the Supporting Information) was successfully detected in both scattering and fluorescence mode (Figure 1b, c) using identical evanescent illumination and image acquisition conditions for both acquisition modes. Except for a few nonfluorescent surface impurities that were visible in the scattering image only, the micrographs of lipid vesicles imaged in these modes (Figure 1b,c) are almost identical, a feature which was utilized below to directly compare the fluorescence and scattering signals originating from individual lipid vesicles.

Distribution in Scattering Intensity of Single Lipid Vesicles Reflects Their Size Distribution. To the first approximation, a surface-immobilized lipid vesicle has a spherical shell-like geometry, and if labeled, the fluorescent molecules can be considered to be evenly distributed in the lipid shell. The number of fluorescent molecules per vesicle is large, and their surface concentration, c, can therefore be considered to be independent of the vesicle radius, r. In this case, the fluorescence intensity, I_f, of a vesicle is determined by the amplitude of the evanescent field and scales as

$$I_f \propto cr\delta[1 - \exp(-2r/\delta)]/2 \quad (1)$$

or

$$I_f \propto cr^2 \text{ at } r \ll \delta \quad (2)$$

where δ is the evanescent field decay length.[36] The dependence of the vesicle's scattering intensity, I_s, on r is somewhat more complicated since it depends on the amplitude and phase of the evanescent field. Mathematically, the scattering can be described in the Rayleigh−Gans−Debye approximation, but the corresponding general expression for I_s is cumbersome (see the Supporting Information). However, to get a

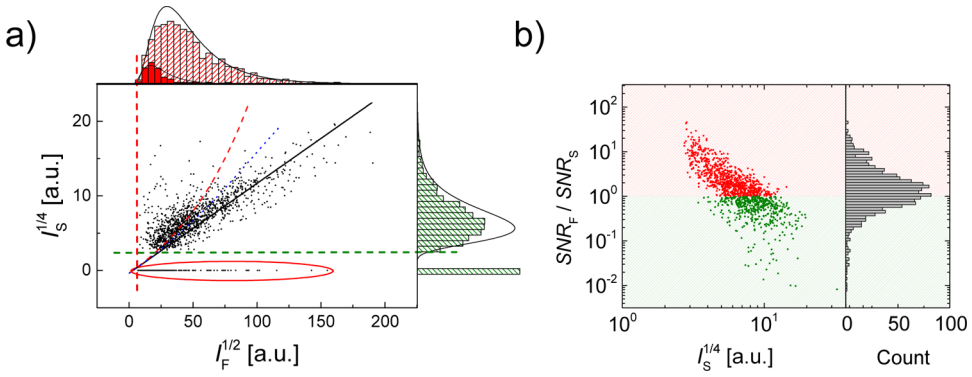

Figure 2. Scattering and fluorescence intensities from single vesicles. (a) Scaling with the powers 1/4 and 1/2 for 2000 single fluorescently labeled vesicles with average diameter of 150 nm. The plot is expected to be linear provided $I_s \propto r^4$ and $I_f \propto r^2$. The distributions of the scattering (green) and fluorescence (red) intensities have been projected onto the *y* and *x* axis, respectively, and correspond to the size distribution of the vesicles. The red vertical and green horizontal dashed lines indicate the limit of detection. The black straight line, red dashed curve, and blue dotted curve show the theoretically predicted behavior according to eqs 2 and 4, 1 and 4, and 1 and 3, respectively. (b) Ratio SNR_f/SNR_s for all measured vesicles as a function of scattering intensity, with the SNR defined as $I_{s/f}/\sigma_{s/f}$, where $\sigma_{s/f}$ is the standard deviation of the background noise. The histogram to the right shows the distribution of this ratio indicating that on average the fluorescence signal gives a better SNR than the scattering signal for these particular vesicles (containing 1 wt % rhodamine−PE lipids) in this size range. It should be noted that the exact crossover-point, where $SNR_f/SNR_s = 1$ in the figure, depends appreciably on the density of fluorescent labels on the vesicles (here 1 wt % rhodamine lipids).

rough estimate, we take only the effect of the amplitude of the evanescent field into account and obtain

$$I_s \propto r^2\delta^2[1 - \exp(-r/\delta)]^2 \quad (3)$$

or

$$I_s \propto r^4, \text{ at } r \ll \delta \quad (4)$$

As expected, eqs 2 and 4 predict that $I_s^{1/4} \propto I_f^{1/2}$ provided $r \ll \delta$. Equations 1 and 3 indicate that this scaling holds up to $r \approx \delta$. The effect of the phase of the evanescent field on the light scattering results in an additional decrease of I_s with increasing r, and accordingly, this scaling is expected to hold for r slightly larger than δ as well. In agreement with these theoretical predictions, our experiments with fluorescently labeled (1 wt % rhodamine−PE) POPC vesicles of the average radius ~75 nm (see the NTA data, Supporting Information, Figure S2) indicate that $I_s^{1/4} \propto I_f^{1/2}$ up to $r \approx 2\delta$ ($\delta \sim 130$ nm) despite relatively broad spreading of the data points (black dots in Figure 2a). Concerning the latter aspect, we note that similar although larger spreading in the fluorescence intensities of lipid vesicles was previously reported[33] using a preparation protocol similar to that employed here. This feature was in that case attributed to inhomogeneous lipid composition in individual vesicles, suggesting that the spreading in our data might also originate from this factor at least partly.

Our measurements also show that a small fraction (<15%) of the vesicles observed in the fluorescence channel did not generate a corresponding detectable scattering signal. A separate analysis of these vesicles (filled red bars in the top histogram on the top *x*-axis) revealed that a majority of them corresponds to weak fluorescence signals; *i.e.*, their size is small. The lower threshold for detecting vesicles in scattering mode is thus close to the modal value of this subdistribution, which from a comparison with an NTA-based size determination of this batch of vesicles (Figure S2) corresponds to a diameter around 80 nm (indicated by a horizontal green dashed line in Figure 2a). This interpretation is supported by a comparison of the signal-to-noise ratio (SNR) of the two modes of operation, which demonstrated a higher SNR ($SNR_f/SNR_s > 1$) in fluorescence mode for weakly scattering (small) vesicles (indicated with red data points on red-shaded area in Figure 2b), while the opposite holds true for strongly scattering objects (indicated with green data points on green-shaded area in Figure 2b). This observation is consistent with the proportionality of I_s and I_f to r^4 and r^2, respectively, since with a constant noise level the scattering intensity is expected to be weaker than the fluorescence intensity for small but stronger for the large vesicles. It is in this context interesting that the absolute signals obtained in scattering and fluorescence modes under identical illumination and imaging conditions were quite different, ranging between 5×10^2 to 2×10^5 and 2×10^2 to 4×10^4 (arbitrary, but comparable, units), respectively. Since in fluorescence mode the mean background signal and the background noise were both low, a further improvement of the SNR in the scattering mode should thus focus on reducing the relatively high noise on the otherwise low mean background signal obtained in scattering mode (see Figure S3 and discussion on SNR in the Supporting Information). To obtain sufficient sensitivity in the studies reported below on label-free detection of protein binding to and phospholipase digestion of single lipid vesicles, the analysis was accordingly restricted to vesicles well visible both in scattering and fluorescence mode.

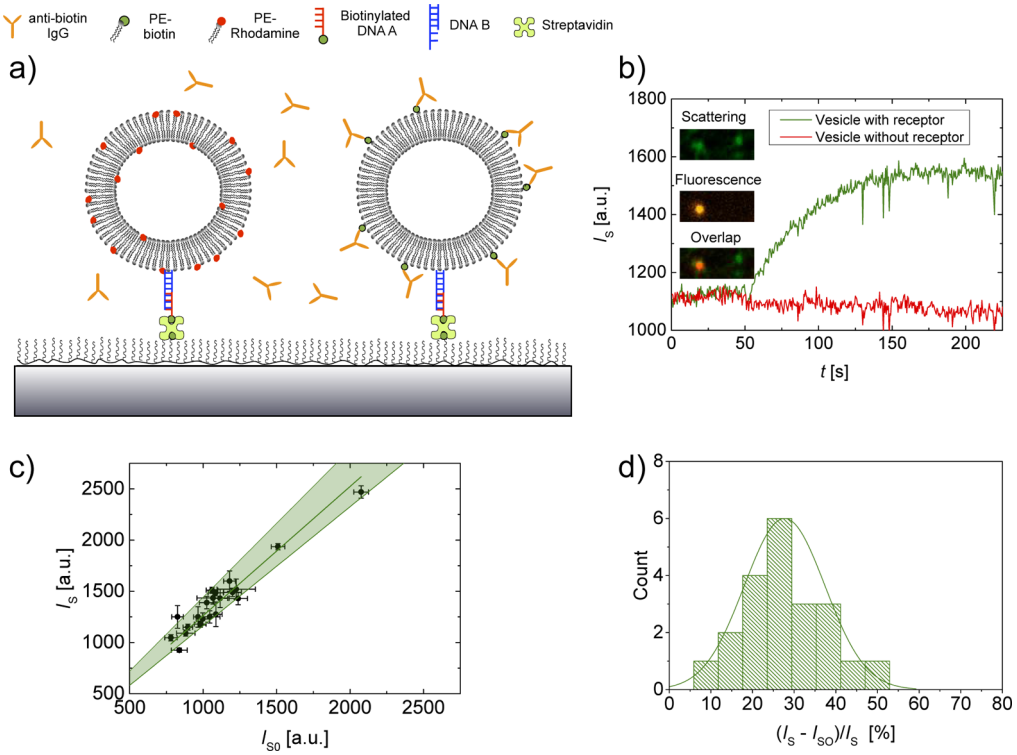

Figure 3. Receptor−ligand interactions on individual vesicles. (a) Two populations of lipid vesicles immobilized on a PLLgPEG surface thorough DNA linking. One vesicle subset (left) contained fluorescent rhodamine while the other (right) contained biotin. (b) The scattering intensity for the two types of vesicles as a function of time upon addition of antibiotin−IgG (injection at t = 50 s). The IgG molecules bound to the biotinylated vesicles resulting in an increase in its scattered signal (green curve), while no increase was observed for the nonbiotinylated vesicle (red curve). The inset micrographs show the two types of surface-immobilized vesicles sitting side-by-side on the functionalized surface obtained in scattering (green) and fluorescence (orange) modes. The insets are approximately 8 μm^2 wide. (c) Single vesicle scattering intensity after IgG binding (I_s) as a function of the vesicle scattering intensity prior to binding (I_{s0}). (d) Distribution of relative scattering signal increased upon IgG binding for all the measured vesicles.

Single-Lipid Vesicle Imaging in Scattering Mode Enables Label-Free Detection of Antibody Binding. Successful label-free detection of individual lipid vesicles suggests that it may also be possible to track biomolecular interactions on individual vesicles by monitoring changes in their scattering intensity, thus excluding implementation of fluorescent labels typically used for this purpose[37] or alternative labeling concepts such as metallic nanoparticles.[38,39] To explore this possibility, the exposed silica region of the waveguide chip was functionalized with a layer of PLL-*g*-PEG/PLL-*g*-PEG-biotin (ratio 1:1) for immobilization of both biotin-containing (10 wt % PE-biotin lipids) and biotin-free, but fluorescently labeled (1 wt % PE-rhodamine lipids), lipid vesicles (nominal diameter ~200 nm). Both types of vesicles were bound using streptavidin and biotin-modified double-stranded cholesterol−DNA as the linker molecules[40] (Figure 3a and Supporting Information). Upon addition of antibiotin IgG (50 nM) to the two types of immobilized lipid vesicles there was a monotonic increase in the scattering signal of the (nonfluorescent) biotin-containing lipid vesicles, while no detectible response was observed for (biotin-free) fluorescently labeled vesicles (Figure 3b), the latter of which was visible in both the scattering and the fluorescence modes, while the former was observed in scattering mode only (inset in Figure 4b). Statistics from ~20 vesicles of each type imaged within a 75 × 75 μm^2 region revealed that the change in I_s of each individual biotin-containing vesicle scaled linearly with their initial scattering intensity, I_{s0} (Figure 3c), with an average increase of 30% normally distributed around the mean value (Figure 3d).

Under the assumption that the scattering intensity is proportional to the square of the mass (Figure 2a) and since the vesicle radius, r, is significantly larger than the membrane thickness, l, the dependence of I_s on a change in membrane thickness, Δl, scales to a first approximation as $r^4(l + \Delta l)^2$, and the slope consequently equals $[(l + \Delta l)/l]^2$. Thus, an increase of $I_s(\Delta l)/I_{s0}$ by 30% (Figure 4d) is expected for $\Delta l/l = 0.15$, which for a membrane thickness of ~5 nm corresponds to an increase in shell thickness of less than 1 nm. Taking into consideration the Y-shaped form (5 × 8 × 10 nm^3) of an IgG molecule,[41] this is a surprisingly low value. Possible explanations to this discrepancy are that the refractive index of proteins is larger than that of lipid membranes, which was neglected in the simplistic estimate above, and/or that the IgG surface coverage is much lower than the theoretical maximum surface

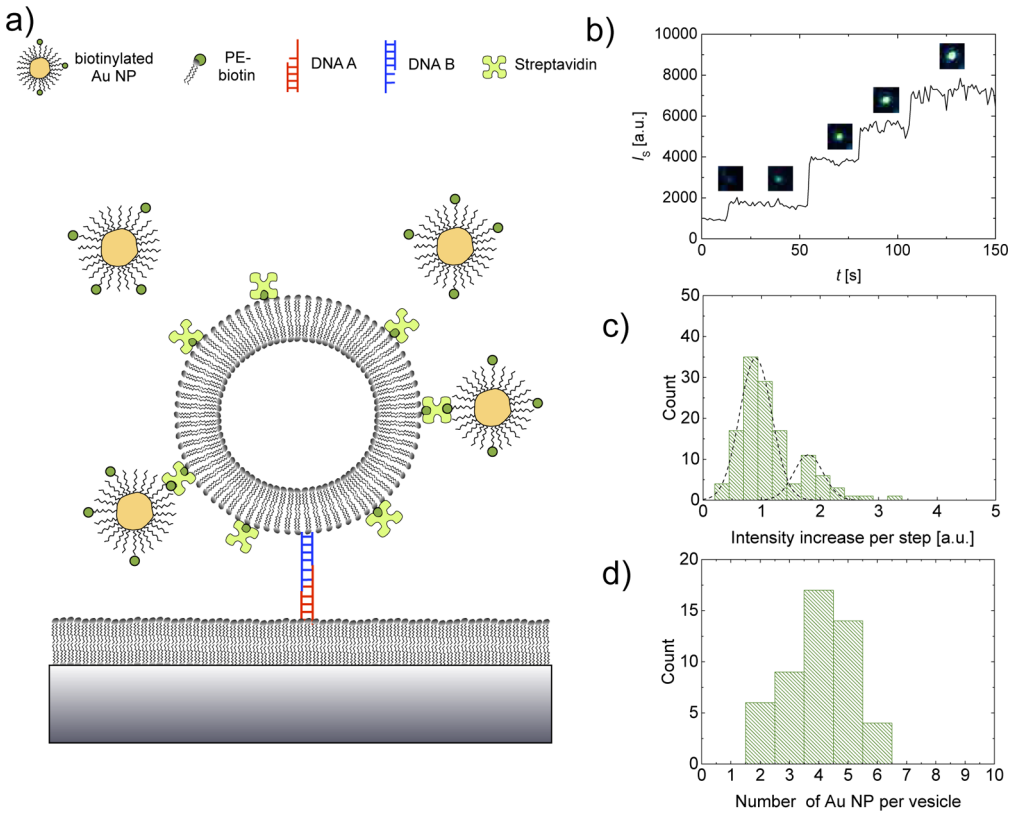

Figure 4. Binding of Au nanoparticles by single vesicles. (a) Schematic representation of the model system for studying molecular binding events using gold NPs as labels. Streptavidin-functionalized vesicles were immobilized to a biotin-free-supported lipid bilayer *via* a DNA linker. (b) Scattering intensity from a single vesicle as a function of time upon binding of 18 nm in diameter biotin-functionalized gold NPs to the vesicle. Upon addition of gold NPs, specific binding of individual NPs to the vesicles was observed, while no binding was observed to the supported lipid bilayer. The inset images are approximately 2 μm wide and show the increasing scattering intensity from the single vesicle at different times during the process. (c) Intensity increase per recorded binding event. Steps appear in multiples of approximately one (arbitrary) intensity unit, indicated by dashed Gaussian-shaped curves. (d) Distribution of the total number of binding events per vesicle. On average, four gold particles were bound to each vesicle within the time frame of the measurements (150 s).

coverage of ~50%,[42] which is likely since a significant fraction of the vesicle is not accessible due to its close proximity to the substrate. Even if this reasoning suggests that the coverage is not complete, it is interesting to note that with a footprint for IgG of at least 50 nm^2 and a maximum coverage of ~50%, saturated binding to a vesicle with a diameter of 200 nm would correspond to a maximum of around 1000 proteins. The signal-to-noise ratio (SNR) of ~30 observed for protein binding to a single lipid vesicle (Figure 4b) thus suggests that ~30 antibodies per vesicle are required for generating a detectable signal (limit of detection). Even if this limit of detection is impressive in terms of the number of molecules needed to get a detectible signal, the limit is, in terms of protein surface coverage, significantly higher than is generally achievable with conventional ensemble-average optical sensors.[43] Although the latter limitation can be partially overcome by averaging over multiple vesicles (SNR $\propto$ [number of vesicles]$^{1/2}$), the power of the single-vesicle approach lies mainly in studies dealing with high-affinity binding to relatively abundant membrane receptors, such as lipids or glycosylated compounds, and to unravel heterogeneities between biological nanoparticles, rather than in detection of rare and/or weakly interacting membrane-bound entities. Motivated by this constraint, we therefore explored the single-molecule detection limit using Au NPs with different size and scattering cross sections.

Detection of Individual Gold Nanoparticle Binding to Single Lipid Vesicles. While label-free detection of single proteins will require an improvement in the sensitivity by up to 1 order of magnitude, metallic NPs with high scattering cross-section were instead explored as signal-enhancing elements to identify single-binding events on preidentified immobilized lipid vesicles. For this purpose, around 50 surface-bound, 100 nm diameter vesicles containing 1 wt % biotinylated lipid modified with streptavidin were imaged in scattering mode upon addition of biotinylated core–shell gold NPs with a diameter of 18 nm (see the Supporting Information), as schematically illustrated in Figure 4a. Binding of gold NPs to individual lipid vesicles resulted in temporally resolved steplike responses, each contributing a similar intensity increase (Figure 4b),

although occasionally a 2-fold increase in intensity was observed (see, *e.g.*, the response between frames 40 and 70 in Figure 4b). Statistics from the entire set of vesicles revealed that the distribution of the intensity increase upon gold NP binding was dominated by single NP binding events, although ~20% of the events corresponded to two NPs (Figure 4c), being attributed to either two binding events occurring within the acquisition time window or to binding of a NP dimer. From the analysis it can also be concluded that, on average, four NPs were observed bending to each vesicle, with the minimum and the maximum number of bound NPs being two and six, respectively (Figure 4d). Taking into account the 10 nm thick PEG corona surrounding the gold NPs, somewhere between 10 and 15 NPs are expected to fit on a single 100 nm lipid vesicle at saturated binding. However, since the part of the vesicle exposed to the substrate, thus being unavailable for binding, is larger here than it is for the significantly smaller IgG molecules (see above) and since multiple bonds can be formed between a NP and streptavidin molecules in the vesicle bilayer, which eventually enwrap the NP and increase the contact area between the particle and vesicle, the real NP loading capacity of each vesicle will decrease with increasing NP coverage (see the Supporting Information). A similar effect was observed upon binding of gold NPs with a core diameter of 25 nm (see the Supporting Information, Figure S6a), while binding of gold NPs with a core diameter of 10 nm resulted in a monotonic, rather than a stepwise increase (see the Supporting Information, Figure S6b), since in this case individual NPs could not be resolved. The observed absolute scattering intensity from individual 18 and 25 nm particles scaled roughly as the square of their volume (r^6), which is in agreement with Rayleigh scattering theory[44] and consistent with the lipid vesicle data (Figure 2a). However, in contrast to the IgG binding to lipid vesicles, there was no strong correlation observed here between the initial scattering intensity of the individual vesicles and the number of bound gold NPs (data not shown), an observation that we tentatively attribute to membrane-wrapping around the gold NPs.

It is also worth noting that the signal fluctuations were observed to increase with each gold−NP binding step (Figure 4b). One possible explanation to this observation is that plasmonic coupling between the gold NPs transiently changes the scattering intensity as the NPs move around on the fluid lipid bilayer membrane of the vesicles. However, such near-field effects are expected to be weak due to the presence of the 10 nm PEG/PEG−biotin polymer shell surrounding the 18 nm gold NPs. Another plausible explanation is therefore that the fluctuations originate from movement of the vesicle-bound gold NPs within the rapidly decaying evanescent field (~130 nm) near the surface. If the latter explanation holds true, measurements of this type open up new means to approach the challenging task of measuring diffusivity of membrane-enveloped nanoscopic biological particles, such as extracellular vesicles including exosomes, and enveloped virions.

Fluorescence and Label-Free Measurements of Phospholipase Digestion of Immobilized Lipid Vesicles Show Correlated Kinetics. Another situation where elimination of fluorescent labeling might be even more important than in protein-binding studies is when fluorescently labeled lipids are used to investigate biophysical properties of the cell membrane, including functional studies of protein− or enzyme−lipid interactions. This concern is particularly relevant because the dye molecules employed to modify lipids usually have dimensions comparable to and physicochemical properties very different from the actual lipids themselves. An example of a biologically and medically important case in which this concern is particularly relevant is in studies of hydrolytic digestion of lipid membranes by phospholipase A2 (PLA2), a processive cell membrane associated enzyme that acts by catalyzing the cleavage of phospholipids. The importance of PLA2 as a biomarker to diagnose diseases, such as cancer and neurodegenerative disorders,[45] or states of diseases, such as inflammatory responses, has made the development of assays capable of probing PLA2 activity a very active research field. In order to reduce the effect of labeling on the reaction kinetics, most sensitive assays engage only a small fraction (1−10%) of head- or tail-labeled fluorescent lipids in a membrane predominantly composed of unlabeled lipids.[34,46] When these lipids are included in unilamellar lipid vesicles, the cleavage by PLA2 of the lipids into a fatty acid and lysophospholipid induces escape of fluorescently labeled products accompanied by a reduction in vesicle size, a process that can be resolved at single vesicles down to the single-enzyme level using fluorescence imaging.[35,46] This PLA2-detection concept was here investigated by addition of PLA2 (250 nM) to fluorescently labeled (1 wt % rhodamine lipids) and biotin-modified (1 wt % biotin lipids) POPC lipid vesicles immobilized to a PLL-gPEG/PLL-*g*-PEG-biotin-modified (10000:1 ratio) silica substrate with NeutrAvidin acting as a linker molecule (Figure 5a). The PLA2 was introduced by pipetting 10 μL of 100 nM PLA2 into the 30 μL TRIS buffer solution, already on the chip, followed by gentle mixing. This resulted in detectable reductions in both I_s (green) and I_f (red) of single vesicles (Figure 5b), revealing that the time-dependent decline of the scattering signal was typically a factor of 2 faster than the corresponding fluorescence signal (see the Supporting Information and Figure S8 for additional single-vesicle traces and the average response, respectively). However, since PLA2 digestion results in a reduction in vesicle size, and since $I_s \propto r^4 I^2$ while $I_f \propto r^2$ (cf. Figure 2), the

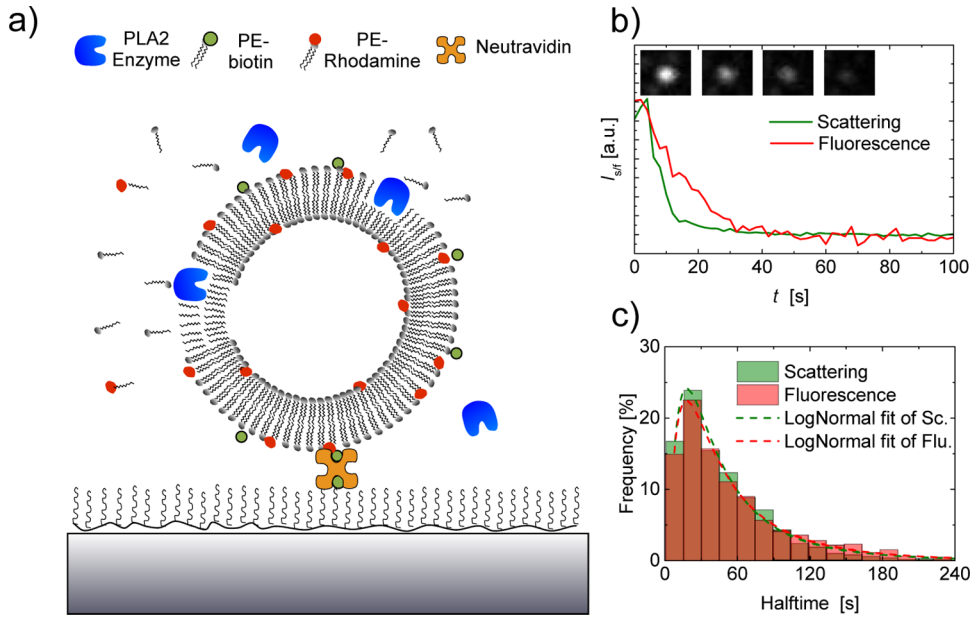

Figure 5. Label-free monitoring of enzyme activity on individual vesicles using both scattering and fluorescence monitoring. (a) Schematic representation of the model system used to monitor the digestion of a single 100 nm immobilized vesicles by the enzyme PLA2 as a function of time. (b) Scattering (green curve) and fluorescence (red curve) intensity of a selected vesicle upon PLA2 digestion. The micrograph insets (2 μm wide) show the corresponding appearance of the fading vesicle as observed in scattering mode at different times during the acquisition. (c) Distribution of halftimes for the measured vesicles extracted from scattering intensities (green bars) and fluorescence intensities (red bars).

emerging result when this is taken into account (see the Supporting Information for details) is that the halftime distributions obtained from I_f and I_s correlate excellently (Figure 5d). This suggests that the dye modification of a small fraction of lipid vesicles has, at least for the particular type of dye used in this case, a negligible influence on the measured digestion rates. Another interesting observation is that with increasing time both I_f and I_s decrease down to negligible values, indicating that the vesicle digestion is nearly complete or at least yields vesicles or aggregates with sizes below our detection limit in both channels.

These results underscore that scattering-based imaging can in many situations be an attractive alternative to both conventional surface-based label-free sensing and fluorescence imaging, in particular when the introduction of fluorescent labels is undesirable or complicated. One such very demanding example is the real-time monitoring of cellular attachment kinetics, in which almost all studies exclusively rely on advanced fluorescence microscopy techniques. As a final illustration of the capacity of the waveguide chip to contribute complementary information also in complex biological processes, we explored the possibility to use the waveguide chip to monitor surface attachment of unlabeled cells.

Diffraction-Limited Scattering Microscopy Reveals Dynamics of Subcellular Features during Platelet Attachment, Spreading, and Activation. Fluorescence imaging executed by surface-confined illumination, predominantly TIRF microscopy, has been extensively used to study subcellular processes occurring at, or in close proximity to, the cell membrane–substrate interface, including, for example, substrate-induced stimuli that induce changes in cell morphology, cell motility, and formation of focal adhesions.[30,47,48] Waveguides have been used for this purpose and, although predominantly in combination with fluorescence labeling,[25,27,49] direct utilization of evanescent-field induced scattering signals for detection of bacterial biofilm growth has also been reported.[31] We were curious to investigate if the low stray light background offered by our waveguide design could allow label-free imaging of cellular attachment in a fashion similar to what is achievable with reflection interference contrast (RIC) microscopy, which enables cellular adhesion to be visualized with subcellular resolution by probing spatial variations near the cell–substrate interface.[50] As a model system, we investigated adhesion and surface-induced activation of platelets, which are micron-sized nuclei-free cellular fragments that play a key role during, for example, blood clotting. In this process, a combination of chemical, mechanical, and/or surface-induced stimuli leads to rapid (within seconds) cytoskeleton reorganization,[50] making it a particularly interesting system to investigate with time-resolved surface-confined label-free microscopy.

Upon exposure of a cleaned but otherwise untreated silica substrate of the waveguide chip to human-derived platelet (thrombocyte) by pipetting (1×10^6 platelets/ml), live imaging initially revealed

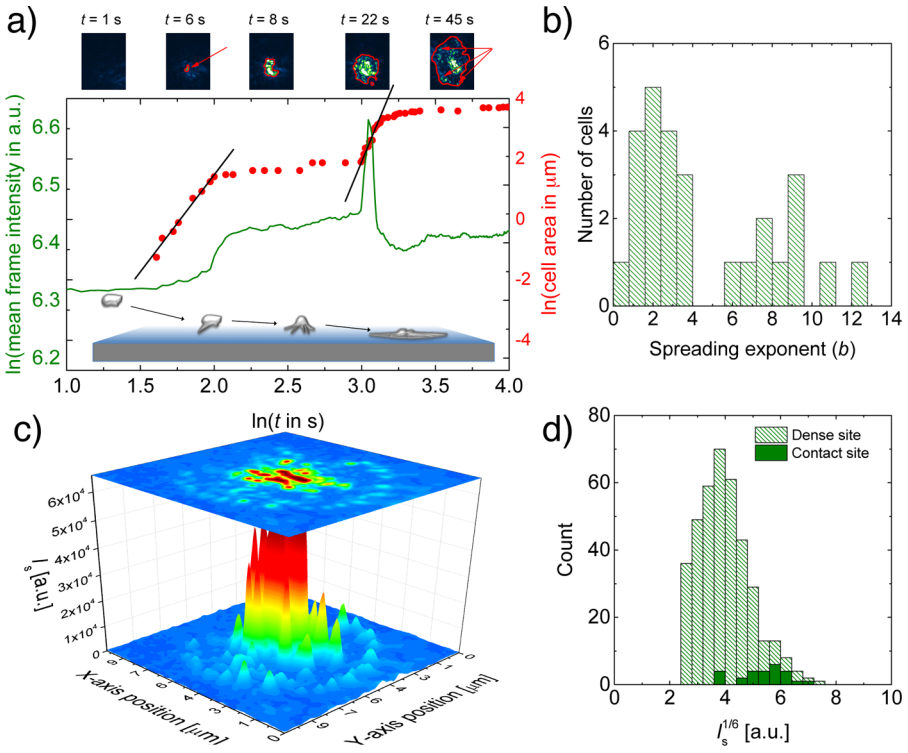

Figure 6. Attachment of a single human-derived platelet to silica. (a) Platelet that cautiously approached the surface, established the first contact with it (t = 6 s), then gradually increased the number of attachment points (6 < t < 22 s) until, in a spontaneous manner, it spread out (t = 22 s), settled down, and reached complete rest (t = 45 s). The red arrows indicate dynamic high-density granules within the filamentous zone of the cell. The inset images are 10 × 14 μm^2. The solid green curve represents the mean scattering intensity detected within the platelets periphery, while the red circles represent the area enclosed by the periphery. (b) Distribution of the contact-area growth exponent b, indicating slow and fast spreading regimes. (c) Three-dimensional intensity plot of an activated platelet indicating the dense sites (with high scattering) within the filamentous zone of the cell and near its edge. (d) Scattering intensity distribution of dense sites after a completed activation (green-shaded bars) and of the initial contact sites (green solid bars).

faint transient features attributed to platelets hovering over the surface mostly outside the evanescent field. A typical platelet then established a single-point contact with the surface, which appeared as a local increase in scattering intensity (red arrow, inset for t = 6 s, Figure 6a). Within seconds, this contact was followed by the formation of additional contact points (inset for t = 8 s, Figure 6a) and a gradual increase in both the mean scattering intensity (solid green line, Figure 6a) and the area enclosed by the periphery of the platelet (red circles, Figure 6a). The initial increase in scattering intensity and growth of the periphery subsequently leveled off for around 10 s, until a transient peak in the mean scattering intensity suddenly appeared, being accompanied by a monotonic increase in the area of the platelet periphery. The growth of contact area (A) of surface-activated platelets has previously been shown to follow a power-law dependence, $A \propto t^b$, where b is the corresponding exponent.[50] The growth profiles were well represented by this relation (black liner regression lines in Figure 6a), and the statistics from ~20 platelets showed that the initial growth phase was always significantly slower (with $1 \leq b \leq 3$) than the final one (with $6 \leq b \leq 12$).

The overall process shown in Figure 6a (see Supporting Information, Figure S10, for a magnified version of Figure 6a and movies SM2, SM3, and SM4 for examples of cell attachments), and the corresponding growth exponents (Figure 6b) are consistent with previous reports on platelet adhesion, activation, and spreading on silica.[50,51] This thus suggests that the transient peak in the scattering intensity originates from surface-induced platelet activation, during which platelets are known to undergo substantial flattening into a morphology resembling a fried egg, with a thin filamentous zone surrounding the central granulomere region.[51] Indeed, a three-dimensional false color surface plot of a fully activated platelet at rest resembles such a structure, with highly scattering (optically dense) sites near the center of the activated platelet being surrounded by a ring of more faint features near the periphery (Figure 6c). A comparison of the scattering intensity of such features, collected from in total ~20 cells (dashed bars in Figure 6d), with the scattering intensity of the initial contact points, collected from the same cells (filled bars in Figure 6d), shows that the latter intensity was similar to the most dense features of the activated cell. This suggests that the point of initial contact is made by an optically dense structure,

such as a protein-rich adhesion region as previously suggested[50,52] (and accordingly it makes sense to use $I_s^{1/6}$ to construct Figure 6d), while the majority of the features distinguished after activation are smaller and/or less optically dense. Curiously, some of the locally distinct regions present in the outer filamentous zone of the platelets after completed activation and spreading remained dynamic throughout the entire measurement (Figure 6a, red arrows in inset at $t = 45$ s and movies SM2, SM3, and SM4). One possible interpretation of this observation is that the fluctuations reflect transport of intracellular granules containing signaling molecules and proteins, which has been suggested to be delivered in this way to cell−substrate contact regions.[53,54] These observations thus extend the aforementioned results on vesicle adhesion by illustrating how label-free surface-confined scattering-microscopy could also serve as an important complement to both RIC and TIRF microscopy by utilizing the possibility to combine scattering microscopy with specific fluorescent labeling of the different molecular machineries involved in adhesion, spreading, and activation processes.

CONCLUSIONS

Key assets of surface-based bioanalytical sensors are high sensitivity, reliable translation of the detected signals into physically meaningful information, compatibility with suitable surface chemistries, as well as simplicity, user friendliness, and low cost. Bearing this in mind, we have in this work demonstrated the applicability of a new type of waveguide chip that through its unique design suppresses background scattering and allows for simple and direct label-free detection of scattered light from surface-immobilized nanoscopic objects interacting with the evanescent light confined to the surfaces of the chip. The chip can also be used in a manner comparable to standard TIRF microscopy and is thus capable of simultaneously monitoring individual objects with fluorescent and scattering read-out. With respect to the sensitivity obtained in the label-free scattering mode, individual lipid vesicles with diameters down to below 100 nm were readily detected, as was specific protein binding to single immobilized vesicles, albeit not with single protein sensitivity. This competes very favorably with previous reports on light-scattering based detection of surface-bound dielectric particles using evanescent illumination,[23] while the increased contrast obtained in interferometric scattering microscopy has been shown to offer an order of magnitude higher sensitivity.[11] The high sensitivity of interferometric scattering microscopy has been attributed to the fact that the read-out signal is generated from the interference between a reference-beam (usually background reflection) and scattered light from the object under study. In this configuration the signal will, under certain conditions, scale with the object's volume rather than the volume squared, thus making the size-dependent decline of the signal less pronounced than for scattered light alone.[9] However, since interferometric scattering microscopy is based on optical interference between reflected light interacting with objects much smaller than the wavelength of light, translation of the detected signals into representative physical properties is more complicated than interpretation of the corresponding dependence of the scattering light intensity, which is often simply proportional to the square of the volume of the detected entities (Figure 2a; see the discussion in the Supporting Information). An attractive approach to further improve the information content of scattering-based microscopy measurements would thus be to take advantage of the direct compatibility of the waveguide chip configuration with any microscope setup, which would enable its direct combination with, *e.g.*, interference-based microscopy. This would aid the use of surface-confined scattering-based microscopy to improve size-distribution determination of nanoscopic particles. Surface-based size determination of nanoscopic particles offers the advantage over bulk-based methods, such as NTA or dynamic light scattering, that only a few hundred particles are sufficient to perform an analysis, which makes the approach particularly attractive for rare or dilute samples, *e.g.*, for size-distribution determination of specific subsets of nanosized biological objects, such as extracellular vesicles, exosomes or virus particles present in crude biological samples. In this case, selective binding to the interface is preferably obtained by specific biorecognition, which requires the surface chemistry to be appropriately controlled.

Previous waveguide designs of the type used in this work employing organic claddings have been restricted to core layers made from high refractive index polymers, such as PMMA.[26] The utilized combination of an organic cladding material (in this work, its refractive index was matched to that of water to reduce background scattering) with an inorganic silica core was proven compatible with conventional surface chemistries developed for silica substrates, as demonstrated here for supported lipid bilayer formation (Figure 4 and Figure S7, Supporting Information), known to be very sensitive to surface imperfections[55] and surface modifications based on electrostatic attraction using polylysine derivatives (Figures 3 and 5). Another advantage of being able to simultaneously identify multiple surface-bound nanoscopic objects is that selective binding to these objects can be verified by identifying colocalized visualization of binding events to individual vesicles, as shown here for selective binding of antibodies and gold NPs to receptors on surface-bound lipid vesicles (Figures 3 and 4). Co-localized detection of this type is particularly beneficial in the context of reducing the parasitic signals originating

from unspecific binding reactions,[56] which typically put strong requirements on minimizing nonspecific binding to the substrate surrounding immobilized lipid vesicles when probed using ensemble-averaging surface-analytical tools, such as quartz crystal microbalance or surface plasmon resonance.[57] By being able to identify the position of individual vesicles (or alternative nanoscopic particles) prior to the binding reaction, nonspecific binding to the vesicle's surrounding becomes less relevant, thus releasing the requisite of producing nearly perfectly inert surface coatings.

Another field that might benefit from the simplicity of the waveguide chip and the compatibility of the silica core layer with various surface chemistries is in the studies of cellular adhesion and motility. The compatibility with a large arsenal of label-free and fluorescence-based microscopy methods allows for novel studies that extend beyond platelet adhesion, activation, and spreading as featured in this work (Figure 6).

In summary, simultaneous observation of scattered and fluorescent light from multiple surface-associated nanoscopic objects using standard microscopes and cameras offers a valuable tool in various biological contexts, since in the absence of labeling agents the biological systems are both intrinsically photostable and less perturbed from their natural state. In future work, we foresee to broaden the applicability of the waveguide chips by making them compatible with microfluidics[58] and integrated optics[59,60] or other lab-on-a-chip functionalities with multiple sensing wells for efficient high throughput, parallel read-out, and improved liquid handling.

METHODS

Fabrication of Waveguide Chips and Surface Functionalization. A single-mode, symmetric planar waveguide structure consisting of a 400 nm thick silica core layer (spin-on-glass, IC1-200 from Futurrex, Inc.) embedded in a 7 μm thick cladding layer of a fluorinated polymer (CYTOP, CTX-809AP2 from AGC Chemicals, ASAHI Glass Co., Ltd.) was fabricated on a standard Si(100) four-inch wafer at the MC2 nanofabrication laboratory, Chalmers, Sweden (Fed. Std.209 E 10-100). All layers were made using spin-casting and subsequent baking in either an oven or on a hot plate. 2×2 mm^2 openings were formed (sample wells or sensing regions) by reactive ion etching in the top cladding layer, exposing the core layer of the waveguide to the environment. The wafer was then diced into 1×1 cm^2 chips, each containing a single sample well. After processing, the chips were cleaned in a NaOH solution (pH 11) for 30 min followed by a gentle rinsing in deionized water for 3 min. The chips were then blow-dried using nitrogen and stored in a cupboard. Prior to all surface modifications and measurements, the surface of the chip was treated for 15 min in O_2 plasma (Harrick Plasma cleaner, 30 W), followed by cleaning in 2 M sulfuric acid (H_2SO_4) for 30 min before subsequent extensive rinsing in Milli-Q water and drying in nitrogen gas.

For preparation of PLL-*g*-PEG-biotin-functionalized surfaces, 1 μg/mL PLL-*g*-PEG (specifically PLL (20)-*g*[3.5]-PEG(2) from SuSOS AG) was mixed with 1 μg/mL PLL-*g*-PEG-biotin (specifically PLL(20)-*g*[3.5]-PEG(2)/PEGbiotin(3.4) 50% from SuSOS AG) in a specific volume ratio to attain 1 μg/mL mixture containing the desired biotin concentration. Approximately 20 μL of the mixed solution (1 μg/mL) was then introduced to the chips surface and left under stagnant conditions for 20 min to incubate. The chip was subsequently rinsed in Milli-Q water.

For the preparation of a PLL surface, a 20 μL of a solution containing 10 μg/mL PLL (specifically poly-L-lysine hydrobromide, 15−30 kDa from Sigma-Aldrich) was introduced to the chip surface and left to incubate under stagnant conditions for 5 min before being rinsed with Milli-Q.

For the preparation of a surface with a supported-lipid bilayer, a solution containing 0.1−0.5 mg/mL unilamellar vesicles, extruded 20 times through a 30 nm polycarbonate membrane (see following section for how the vesicles were prepared), was added to the chip and allowed to incubate until a bilayer had formed. The successful bilayer formation was confirmed by monitoring the whole process, from vesicle adsorption to fusion into bilayer, in scattering mode.

Preparation of Lipid Vesicles and DNA Modification of Vesicles. Five different types of (1 mg/mL) unilamellar lipid vesicles were prepared for the experiments describe in this article. All types had 1-palmitoyl-2-oleoyl-*sn*-glycero-3-phosphocholine (POPC, Avanti Polar Lipids) as a main constituent with additional components added in specific ratios to achieve the desired modification. For preparation of rhodamine- or NBD-labeled vesicles, POPC lipids were mixed with either lissamine rhodamine B 1,2-dihexadecanoyl-*sn*-glycero-3-phosphatidylethanolamine (rhodamine−DHPE, Invitrogen) or 2-(12-(7-nitrobenz-2-oxa-1,3-diazol-4-yl)amino)dodecanoyl-1-hexadecanoyl-*sn*-glycero-3-phosphocholine (NBD C12-HPC, Invitrogen) in ratios of 98 wt % POPC to 2 wt % label or 99 wt % POPC to 1 wt % label. For preparation of biotinylated vesicles, 99 wt % POPC were mixed with 1 wt % 1,2-dioleoyl-*sn*-glycero-3-phosphoethanolamine-*N*-(biotinyl) (biotin-PE, Avanti Polar Lipids). The vesicles containing both biotin and rhodamine were prepared by mixing 98 wt % POPC with 1 wt % rhodamine−DHPE and 1 wt % biotin−PE.

After mixing with labels and/or biotin−PE, the lipids were dissolved in methanol and subsequently dried in vacuum for 1 h before being rehydrated in either PBS or TRIS buffer with pH 7.4 and vortexed for 5 min. The suspensions were then extruded 20 times through a polycarbonate membrane (Whatman) with 30, 100, or 200 nm pore sized depending on application (see Figure S2 in the Supporting Information for typical size distribution of POPC vesicles in bulk). Finally, the vesicle suspensions were stored at 4 °C in a fridge.

To produce DNA-modified vesicles, the desired vesicle suspension was incubated for 30 min with a bicholesterol-modified DNA (DNA-B) construct (Eurogentec) at a DNA/vesicle ratio of 8:1 just prior to the experiment. The 15 bases single stranded overhang on the cholesterol-DNA construct is complementary to a DNA strand (DNA-A), which was immobilized on the chip surface either using biotin or bicholesterol in a supported lipid bilayer (see below with active nucleobases that form the binding through pairing shown in red).

Vesicle Bicholesterol-DNA (DNA-B). 5′-TGG-ACA-TCA-GAA-ATA-AGG-CAC-GAC-GGA-CCC-cholesterol-3′

5′-cholesterol-CCC-TCC-GTC-GTG-CCT-3′

Surface-Immobilized Complementary-DNA (DNA-A). 5′-TAT-TTC-TGA-TGT-CCA-CCC-biotin-3′

or

5′-TAT-TTC-TGA-TGT-CCA-AGG-CAC-GAC-GGA-CCC-cholesterol-3′

5′-cholesterol-CCC-TCC-GTC-GTG-CCT-3′

IgG Binding to Surface-Immobilized Lipid Vesicles. PBS buffer with pH 7.4 was used throughout the experiment. After standard cleaning, the chip surface was functionalized with PLL-*g*-PEG/PLL-*g*-PEGbiotin (1000:1 ratio, 10 μg/mL, SuSOS AG), which rapidly formed, by self-assembly, a protein and lipid vesicle resistant polymer layer. Biotinylated-DNA was preincubated with NeutrAvidin (10 μg/mL, Sigma-Aldrich) at a 2:1 DNA/protein ratio and bound to the surface. After subsequent

rinsing, the binding of DNA-modified vesicles (0.1 μg/mL) containing either rhodamine or biotin-lipids was monitored in real time until a sufficient coverage of vesicles (typically a few hundred vesicles) was reached after which the surface was rinsed. The scattering intensity of each individual vesicle was then monitored in real-time upon injection of antibiotin−IgG (10 μg/mL, mouse IgG2a, BioLegend) at a frame rate of 2 frames per second.

Synthesis of Gold Nanoparticles. Gold NPs (10, 18, and 25 nm in diameter) were prepared by citrate reduction of chloroauric acid with addition of tannic acid as extra reductive agent. All glassware was cleaned in a mixture of 1:1:5 of H_2O_2 (30%), NH_3 (25%) and water at 85 °C for 10 min and then rinsed with pure water before use. A 80 mL water solution of $HAuCl_4$ (Aldrich 99.999%) 0.32 mM and a 20 mL solution of sodium citrate (Sigma ACS reagent >99.0%) 6.8 mM with variable concentration of tannic acid (Sigma-Aldrich A.C.S reagent) 0.24 mM for 10 nm particles, 0.015 mM for 18 nm particles, and 0.003 mM for 25 nm particles was heated under gentle stirring. When the temperature reached 60 °C, the two solutions were mixed whereupon the mixture changed color to almost black, purple, and finally dark red after approximately 30 min for 10 nm particles, 90 min for 18 nm particles and several hours for 25 nm particles. The solution was then first quickly heated to 95 °C and then cooled on ice. The final volume was adjusted to 100 mL using pure water. These NPs are charge stabilized, and the particle sols will remain stable at pH >4 and ionic strengths <10 mM for extended times when refrigerated. The NPs size was determined using scanning electron microscopy (SEM) and dynamic light scattering (DLS) (see the Supporting Information, Figure S4a,b).

Preparation of Biotin-Modified Gold Nanoparticles. To modify gold NPs with biotin and simultaneously minimize unspecific interaction between NPs and the waveguide surface, the gold NPs, synthesized as described in the previous section, were modified with a mixed monolayer of thiol-conjugated polyethylene glycol and polyethylene glycol biotin. A stock solution containing a mixture of 50% SH-PEG MW5000 Da (Fluka), 25% SH-PEG-COO^- MW5000 Da (Rapp Polymere), and 25% SH-PEG-biotin MW5000 Da (Rapp Polymere) was prepared in water to have a total PEG−thiol concentration 1 mM. This solution was quickly added to the NPs sols to a final concentration of 10 μM for 10 nm NPs and 20 μM for 18 and 25 nm NPs. After incubation overnight in a refrigerator (4 °C), the surface-modified NPs were separated from excess thiol-PEG by centrifugation at 20000*g* for 10 nm NPs, 7500*g* for 18 nm NPs, and 3500*g* for 25 nm NPs, whereupon the pellet was diluted in Milli-Q water. This procedure was repeated 5 times so that the theoretical background concentration of free SH-PEG-biotin in the NPs sol was less than 1×10^{-14} M. The mono-dispersivity of the NPs after modification with SH-PEG was verified by DLS (data not shown).

Human-Derived Platelets on Silica. The platelet-containing solution was derived from blood donors at the Regional Blood Bank at Sahlgrenska University Hospital, Gothenburg, Sweden, as described in ref 61. The solution of platelets was washed by centrifugation in order to minimize the free protein content in the platelet solution, which upon adsorption to the chips' surface might induce unwanted background scattering. After washing, the stock solution contained 460×10^9 platelets/liter stored in PAS (platelet additive solution, 2.94 g of NaCitrat $\times$ $2H_2O$, 4.08 g of NaAcetat $\times$ $3H_2O$, 6.75 g of NaCl ad 1000 mL, pH 7.2). Before running the experiment, a part of the stock solution was diluted in TRIS 1:100 (460×10^7 platelets/liter) and then 5 μL of that solution was mixed with 20 μL TRIS already on the waveguide chip (100×10^7 platelets/liter).

Conflict of Interest: The authors declare no competing financial interest.

Acknowledgment. This work was funded by the Swedish Research Council, VINNOVA, SSF, the Göran Gustafsson foundation, the Dorothea Schlözer-Programm of Georg-August-University Göttingen, and the EMRP project HLT04 "BioSurf". The EMRP is jointly funded by the EMRP participating countries within EURAMET and the European Union. We thank the staff at the MC2 cleanroom facilities, Chalmers, Gothenburg, for all their help and good advice for the fabrication of the waveguide chip, Dr. Camilla Hesse, for providing the platelets, Dr. Geir Agnarsson for mathematical consultancy, and Dr. Kristján Leósson for general comments.

Supporting Information Available: The Supporting Information is available free of charge on the ACS Publications website at DOI: 10.1021/acsnano.5b04168.

Theoretical background of the optical measurements and supplementary results(PDF)
Cell attachment movie SM1 (AVI)
Cell attachment movie SM2 (AVI)
Cell attachment movie SM3 (AVI)
Cell attachment movie SM4 (AVI)

REFERENCES AND NOTES

1. Weiss, S. Fluorescence Spectroscopy of Single Biomolecules. *Science* **1999**, *283*, 1676–1683.
2. Walt, D. R. Optical Methods for Single Molecule Detection and Analysis. *Anal. Chem.* **2013**, *85*, 1258–1263.
3. Cordes, T.; Blum, S. A. Opportunities and Challenges in Single-Molecule and Single-Particle Fluorescence Microscopy for Mechanistic Studies of Chemical Reactions. *Nat. Chem.* **2013**, *5*, 993–999.
4. Holzmeister, P.; Acuna, G. P.; Grohmann, D.; Tinnefeld, P. Breaking the Concentration Limit of Optical Single-Molecule Detection. *Chem. Soc. Rev.* **2014**, *43*, 1014–1028.
5. Gunnarsson, A.; Snijder, A.; Hicks, J.; Gunnarsson, J.; Höök, F.; Geschwindner, S. Drug Discovery at the Single Molecule Level: Inhibition-in-Solution Assay of Membrane-Reconstituted B-Secretase Using Single-Molecule Imaging. *Anal. Chem.* **2015**, *87*, 4100–4103.
6. van Oijen, A. M. Single-Molecule Approaches to Characterizing Kinetics of Biomolecular Interactions. *Curr. Opin. Biotechnol.* **2011**, *22*, 75–80.
7. Pinaud, F.; Clarke, S.; Sittner, A.; Dahan, M. Probing Cellular Events, One Quantum Dot at a Time. *Nat. Methods* **2010**, *7*, 275–85.
8. Leduc, C.; Si, S.; Gautier, J.; Soto-Ribeiro, M.; Wehrle-Haller, B.; Gautreau, A.; Giannone, G.; Cognet, L.; Lounis, B. A Highly Specific Gold Nanoprobe for Live-Cell Single-Molecule Imaging. *Nano Lett.* **2013**, *13*, 1489–1494.
9. Lindfors, K.; Kalkbrenner, T.; Stoller, P.; Sandoghdar, V. Detection and Spectroscopy of Gold Nanoparticles Using Supercontinuum White Light Confocal Microscopy. *Phys. Rev. Lett.* **2004**, *93*, 037401.
10. Jacobsen, V.; Stoller, P.; Brunner, C.; Vogel, V.; Sandoghdar, V. Interferometric Optical Detection and Tracking of Very Small Gold Nanoparticles at a Water-Glass Interface. *Opt. Express* **2006**, *14*, 405–414.
11. Ewers, H.; Jacobsen, V.; Klotzsch, E.; Smith, A. E.; Helenius, A.; Sandoghdar, V. Label-Free Optical Detection and Tracking of Single Virions Bound to Their Receptors in Supported Membrane Bilayers. *Nano Lett.* **2007**, *7*, 2263–2266.
12. Kukura, P.; Ewers, H.; Müller, C.; Renn, A.; Helenius, A.; Sandoghdar, V. High-Speed Nanoscopic Tracking of the Position and Orientation of a Single Virus. *Nat. Methods* **2009**, *6*, 923–927.
13. Daaboul, G. G.; Yurt, A.; Zhang, X.; Hwang, G. M.; Goldberg, B. B.; Unlü, M. S. High-Throughput Detection and Sizing of Individual Low-Index Nanoparticles and Viruses for Pathogen Identification. *Nano Lett.* **2010**, *10*, 4727–4731.
14. Andrecka, J.; Spillane, K. M.; Ortega-Arroyo, J.; Kukura, P. Direct Observation and Control of Supported Lipid Bilayer Formation with Interferometric Scattering Microscopy. *ACS Nano* **2013**, *7*, 10662–10670.
15. Ortega Arroyo, J.; Andrecka, J.; Spillane, K. M.; Billington, N.; Takagi, Y.; Sellers, J. R.; Kukura, P. Label-Free, All-Optical Detection, Imaging, and Tracking of a Single Protein. *Nano Lett.* **2014**, *14*, 2065–2070.
16. Piliarik, M.; Sandoghdar, V. Direct Optical Sensing of Single Unlabelled Proteins and Super-Resolution Imaging of Their Binding Sites. *Nat. Commun.* **2014**, *5*, 05495.

17. Fang, X.; Tan, W. Imaging Single Fluorescent Molecules at the Interface of an Optical Fiber Probe by Evanescent Wave Excitation. *Anal. Chem.* **1999**, *71*, 3101–3105.
18. Mashanov, G. I.; Tacon, D.; Knight, A. E.; Peckham, M.; Molloy, J. E. Visualizing Single Molecules inside Living Cells Using Total Internal Reflection Fluorescence Microscopy. *Methods* **2003**, *29*, 142–152.
19. Schneckenburger, H. Total Internal Reflection Fluorescence Microscopy: Technical Innovations and Novel Applications. *Curr. Opin. Biotechnol.* **2005**, *16*, 13–18.
20. Loveland, A. B.; Habuchi, S.; Walter, J. C.; van Oijen, A. M. A General Approach to Break the Concentration Barrier in Single-Molecule Imaging. *Nat. Methods* **2012**, *9*, 987–992.
21. He, H.; Ren, J. A Novel Evanescent Wave Scattering Imaging Method for Single Gold Particle Tracking in Solution and on Cell Membrane. *Talanta* **2008**, *77*, 166–171.
22. Ueno, H.; Nishikawa, S.; Iino, R.; Tabata, K. V.; Sakakihara, S.; Yanagida, T.; Noji, H. Simple Dark-Field Microscopy with Nanometer Spatial Precision and Microsecond Temporal Resolution. *Biophys. J.* **2010**, *98*, 2014–2023.
23. Enoki, S.; Iino, R.; Morone, N.; Kaihatsu, K.; Sakakihara, S.; Kato, N.; Noji, H. Label-Free Single-Particle Imaging of the Influenza Virus by Objective-Type Total Internal Reflection Dark-Field Microscopy. *PLoS One* **2012**, *7*, e49208.
24. Thoma, F.; Langein, U.; Mittler-Neher, S. Waveguide Scattering Microscopy. *Opt. Commun.* **1997**, *134*, 16–20.
25. Grandin, H. M.; Städler, B.; Textor, M.; Vörös, J. Waveguide Excitation Fluorescence Microscopy: A New Tool for Sensing and Imaging the Biointerface. *Biosens. Bioelectron.* **2006**, *21*, 1476–1482.
26. Agnarsson, B.; Ingthorsson, S.; Gudjonsson, T.; Leosson, K. Evanescent-Wave Fluorescence Microscopy Using Symmetric Planar Waveguides. *Opt. Express* **2009**, *17*, 5075–5082.
27. Hassanzadeh, A.; Ma, H. K.; Dixon, S. J.; Mittler, S. Visualization of the Solubilization Process of the Plasma Membrane of a Living Cell by Waveguide Evanescent Field Fluorescence Microscopy. *J. Biomed. Opt.* **2012**, *17*, 0760251.
28. Ramachandran, S.; Cohen, D. A.; Quist, A. P.; Lal, R. High Performance, Led Powered, Waveguide Based Total Internal Reflection Microscopy. *Sci. Rep.* **2013**, *3*, 2133.
29. Hassanzadeh, A.; Nitsche, M.; Mittler, S.; Armstrong, S.; Dixon, J.; Langbein, U. Waveguide Evanescent Field Fluorescence Microscopy: Thin Film Fluorescence Intensities and its Application in Cell Biology. *Appl. Phys. Lett.* **2008**, *92*, 233503.
30. Mattheyses, A. L.; Simon, S. M.; Rappoport, J. Z. Imaging with Total Internal Reflection Fluorescence Microscopy for the Cell Biologist. *J. Cell Sci.* **2010**, *123*, 3621–3628.
31. Nahar, Q.; Fleissner, F.; Shuster, J.; Morawitz, M.; Halfpap, C.; Stefan, M.; Langbein, U.; Southam, G.; Mittler, S. Waveguide Evanescent Field Scattering Microscopy: Bacterial Biofilms and Their Sterilization Response via UV Irradiation. *J. Biophotonics* **2014**, *7*, 542–51.
32. Klein, A. *Propulsion of Micro-Sized Objects by the Evanescent Field of an Optical Waveguide*; Fachhochschule: Wiesbaden, 2008.
33. Larsen, J.; Hatzakis, N. S.; Stamou, D. Observation of Inhomogeneity in the Lipid Composition of Individual Nanoscale Liposomes. *J. Am. Chem. Soc.* **2011**, *133*, 10685–10687.
34. Chalbot, S.; Zetterberg, H.; Blennow, K.; Fladby, T.; Grundke-Iqbal, I.; Iqbal, K. Cerebrospinal Fluid Secretory Ca^{2+}-Dependent Phospholipase A2 Activity is Increased in Alzheimer Disease. *Clin. Chem.* **2009**, *55*, 2171–2179.
35. Rabe, M.; Tabaei, S. R.; Zetterberg, H.; Zhdanov, V. P.; Hook, F. Hydrolysis of a Lipid Membrane by Single Enzyme Molecules: Accurate Determination of Kinetic Parameters. *Angew. Chem., Int. Ed.* **2015**, *54*, 1022–1026.
36. Olsson, T.; Zhdanov, V. P.; Höök, F. Total Internal Reflection Fluorescence Microscopy for Determination of Size of Individual Immobilized Vesicles: Theory and Experiment. *J. Appl. Phys.* **2015**, *118*, 064702.
37. Christensen, S. M.; Stamou, D. Surface-Based Lipid Vesicle Reactor Systems: Fabrication and Applications. *Soft Matter* **2007**, *3*, 828–836.
38. Rosi, N. L.; Mirkin, C. A. Nanostructures in Biodiagnostics. *Chem. Rev.* **2005**, *105*, 1547–1562.
39. Jain, P. K.; Huang, X.; El-Sayed, I. H.; El-Sayed, M. A. Noble Metals on the Nanoscale: Optical and Photothermal Properties and Some Applications in Imaging, Sensing, Biology, and Medicine. *Acc. Chem. Res.* **2008**, *41*, 1578–1586.
40. Gunnarsson, A.; Jonsson, P.; Marie, R.; Tegenfeldt, J. O.; Höök, F. Single-Molecule Detection and Mismatch Discrimination of Unlabeled DNA Targets. *Nano Lett.* **2008**, *8*, 183–188.
41. Davies, D. R.; Padlan, E. A.; Segal, D. Three-Dimensional Structure of Immunoglobulins. *Annu. Rev. Biochem.* **1975**, *44*, 639–667.
42. Adamczyk, Z.; Weronski, P.; Musiał, E. Particle Adsorption under Irreversible Conditions: Kinetics and Jamming Coverage. *Colloids Surf., A* **2002**, *208*, 29–40.
43. Estevez, M. C.; Alvarez, M.; Lechuga, L. M. Integrated Optical Devices for Lab-on-a-Chip Biosensing Applications. *Laser Photonics Rev.* **2012**, *6*, 463–487.
44. Yguerabide, J.; Yguerabide, E. E. Light-Scattering Submicroscopic Particles as Highly Fluorescent Analogs and Their Use as Tracer Labels in Clinical and Biological Applications. *Anal. Biochem.* **1998**, *262*, 137–156.
45. Lambeau, G.; Gelb, M. H. Biochemistry and Physiology of Mammalian Secreted Phospholipases A2. *Annu. Rev. Biochem.* **2008**, *77*, 495–520.
46. Tabaei, S. R.; Rabe, M.; Zetterberg, H.; Zhdanov, V. P.; Höök, F. Single Lipid Vesicle Assay for Characterizing Single-Enzyme Kinetics of Phospholipid Hydrolysis in a Complex Biological Fluid. *J. Am. Chem. Soc.* **2013**, *135*, 14151–14158.
47. Axelrod, D. Total Internal Reflection Fluorescence Microscopy in Cell Biology. *Tra□c* **2001**, *2*, 764–774.
48. Toomre, D.; Manstein, D. J. Lighting up the Cell Surface with Evanescent Wave Microscopy. *Trends Cell Biol.* **2001**, *11*, 298–303.
49. Hassanzadeh, A.; Nitsche, M.; Armstrong, S.; Nabavi, N.; Harrison, R.; Dixon, S. J.; Langbein, U.; Mittler, S. Optical Waveguides Formed by Silver Ion Exchange in Schott SG11 Glass for Waveguide Evanescent Field Fluorescence Microscopy: Evanescent Images of HEK293 Cells. *J. Biomed. Opt.* **2010**, *15*, 036018.
50. Lee, D.; Fong, K. P.; King, M. R.; Brass, L. F.; Hammer, D. A. Differential Dynamics of Platelet Contact and Spreading. *Biophys. J.* **2012**, *102*, 472–482.
51. Rodrigues, S. N.; Gonçalves, I. C.; Martins, M. C.; Barbosa, M. A.; Ratner, B. D. Fibrinogen Adsorption, Platelet Adhesion and Activation on Mixed Hydroxyl-/Methyl- Terminated Self-Assembled Monolayers. *Biomaterials* **2006**, *27*, 5357–5367.
52. Jirousková, M. t.; Jaiswal, J. K.; Coller, B. S. Ligand Density Dramatically Affects Integrin αIIbβ3-Mediated Platelet Signaling and Spreading. *Blood* **2007**, *109*, 5260–5269.
53. Li, Z.; Kim, E. S.; Bearer, E. L. Arp2/3 Complex is Required for Actin Polymerization During Platelet Shape Change. *Blood* **2002**, *99*, 4466–4474.
54. Italiano, J. E.; Richardson, J. L.; Patel-Hett, S.; Battinelli, E.; Zaslavsky, A.; Short, S.; Ryeom, S.; Folkman, J.; Klement, G. L. Angiogenesis is Regulated by a Novel Mechanism: Pro- and Antiangiogenic Proteins are Organized into Separate Platelet Alpha Granules and Differentially Released. *Blood* **2007**, *111*, 1227–1233.
55. Cho, N.-J.; Frank, C. W.; Kasemo, B.; Höök, F. Quartz Crystal Microbalance with Dissipation Monitoring of Supported Lipid Bilayers on Various Substrates. *Nat. Protoc.* **2010**, *5*, 1096–1106.
56. Agrawal, A.; Deo, R.; Wang, G. D.; Wang, M. D.; Nie, S. Nanometer-Scale Mapping and Single-Molecule Detection with Color-Coded Nanoparticle Probes. *Proc. Natl. Acad. Sci. U. S. A.* **2008**, *105*, 3298–3303.
57. Cooper, M. A. Advances in Membrane Receptor Screening and Analysis. *J. Mol. Recognit.* **2004**, *17*, 286–315.

58. Leosson, K.; Agnarsson, B. Integrated Biophotonics with Cytop. *Micromachines* **2012**, *3*, 114–125.
59. Halldorsson, J.; Arnfinnsdottir, N. B.; Jonsdottir, A. B.; Agnarsson, B.; Leosson, K. High Index Contrast Polymer Waveguide Platform for Integrated Biophotonics. *Opt. Express* **2010**, *18*, 16217–16226.
60. Agnarsson, B.; Jonsdottir, A. B.; Arnfinnsdottir, N. B.; Leosson, K. On-Chip Modulation of Evanescent Illumination and Live-Cell Imaging with Polymer Waveguides. *Opt. Express* **2011**, *19*, 22929–22935.
61. Kunze, A.; Hesse, C.; Svedhem, S. Real-Time Monitoring of Surface-Confined Platelet Activation on TiO_2. *Colloids Surf., B* **2014**, *116*, 446–51.